4th IAA Planetary Defense Conference – PDC 2015
13-17 April 2015, Frascati, Roma, Italy

IAA-PDC-15-05-02

BREAK-UP MODELLING AND TRAJECTORY SIMULATION UNDER UNCERTAINTY FOR ASTEROIDS

Piyush M. Mehta[(1)], **Edmondo Minisci**[(2)], **and Massimiliano Vasile**[(3)]
University of Strathclyde, Glasgow G1 1XJ, +44 141 5745166,

Keywords: *Re-Entry, Break-up, Uncertainty treatment, ground impact*

ABSTRACT

Near Earth Objects (NEOs) pose a very real and severe threat to the Earth population. The recent event in Chelyabinsk highlights the nature of such a threat. Casualty avoidance and decision making for ground impact require credible and realistic modeling of breakup events and post-breakup trajectory simulations. We present the development of the framework for FOSTRAD (Free Open-Source Tool for Re-entry of Asteroids and Debris) that will allow the survivability analysis of entry objects. FOSTRAD will integrate a multi-fidelity tool for the rapid computation of aerodynamic, aerothermodynamic and thermo-structural properties of entry objects (spacecraft, space debris, and asteroid) with a trajectory propagator to simulate the evolution of the objects from the point of atmospheric entry to the final event that can be either the ground impact or the disintegration and burn-up during the atmospheric flight. The module devoted to the analysis of the asteroid entry incorporates ablation due to convective and radiative heat transfer, fragmentation, post-fragmentation strength model, and fragment interaction and lateral velocity model that links the transverse velocity of the fragments to their relative size. The uncertainties affecting this kind of simulations, such as on the entry conditions and the mechanical properties of the asteroids, is characterized and the tool also provides uncertainty quantification and propagation analysis to have a probabilistic characterization of the final event. In this paper, the tool is applied to an asteroid with characteristics similar to the Chelyabinsk event using the incorporated models and results are presented.

INTRODUCTION

Near Earth Objects (NEOs) are defined as objects in the solar system that have a close proximity to Earth during some part of their orbital motion around the Sun. On February 15, 2013, an asteroid entered Earth's atmosphere with a velocity of ~65,000 km/h and exploded at around 25 km altitude due to the heating and stresses. The asteroid was estimated to have a diameter of ~18 m and a mass of ~11,000 tons. The total energy released to the atmosphere was around 500 kilotons of TNT. The explosion resulting from the immense heating during atmospheric entry resulted in a heat wave and a strong shock wave shattering glass across several miles with approximately 1500 people requiring medical attention. The casualties

could have been much worse had the asteroid survived and reached the Earth's surface. Such an event is estimated to occur roughly on average once every 100 years [1-4].
On the same day, another asteroid 2012DA14 with a diameter of approximately 40 m passed by the Earth at an altitude of only 28,000 km. Impact of asteroids of this size are expected roughly on average every 1000 years [1-4]. These events show that NEOs pose an infrequent, but very real threat to the Earth inhabitants. Survivability and Earth surface impact location of such objects is dictated by, among other things, the atmospheric entry conditions, atmospheric properties and asteroid properties. Unfortunately, almost all parameters that affect survivability and trajectory are uncertain and require uncertainty quantification and propagation (UQ&P) for a realistic modeling of the effects on ground.
In the current work, we present the development and results of a tool that can model and simulate ablation, burn-up/evaporation, fragmentation, pre- and post-fragmentation event trajectories and ground impact footprint as a result of the associated UQ&P. We use a conservative approach by using models for successive fragmentation under the assumption that in the event of an airburst, most of the fragmented pieces would burn up and not make it to the ground. The goal of the current work is to give the most accurate rapid, conservative solution achievable for decisions concerning evacuations for casualty avoidance in case of such an event. Additional secondary effects like shock and heat waves that can also affect the ground-based population are beyond the scope of this work and not considered here.
Study of disintegration of large celestial bodies in the atmosphere is of great interest to the management community for disaster monitoring and decision-making. One of the motivating factors for such a study is the simulation of ground impact and casualty avoidance. Complex physical phenomena such as hypersonic aerodynamics, heating, ablation, fragmentation, interaction between fragments and airbursts describe the passage of a celestial object through the atmosphere. The highly uncertain nature of parameters associated with the atmospheric passage warrants the need for probabilistic modeling of atmospheric trajectory and the physical processes that are encountered.
In the past, modeling of the physical processes has been achieved through numerical and/or analytical methods [5-8]; however, these models can only be used as nominal solutions. An accurate knowledge and prediction of ground impact and casualty for decision-making can be achieved only through uncertainty treatment. The paper is structured as follows: the next section will describe the methodology, with sub-sections that go into detail about the models and physics, followed by a section with results and discussion. The last section will provide conclusions and direction for future work.

METHODOLOGY

We begin the atmospheric entry simulation at an altitude of 120 km. The original parent and all subsequent fragments are modeled as spherical objects. The original parent object is tracked through the atmosphere either down to ground or evaporation due to ablation. Ablation due to convective and radiative heat transfer is modeled. Radiative and convective heat fluxes are calculated through a combination of experimental/computational data and analytical models [9]. The ablation model as

described by Bronshten is used where the effective heat transfer is calculated and translated to rate of change of mass [10]. Fragmentation criteria as developed by Tsvetkov and Skripnik is used to model fragmentation events [11]. Successive fragmentation events are modeled where the parent keeps its original trajectory, whereas, the fragment is given a lateral velocity for separation [12]. Ablation and fragmentation criteria are applied to each subsequent fragment. All subsequent fragment objects are also tracked either to ground impact or evaporation. Figure 1(a) and (b) show a schematic of the trajectory propagation with fragmentation and ablation and a schematic of the planar entry, respectively. Figure 1(c) shows the algorithm developed for the simulation.

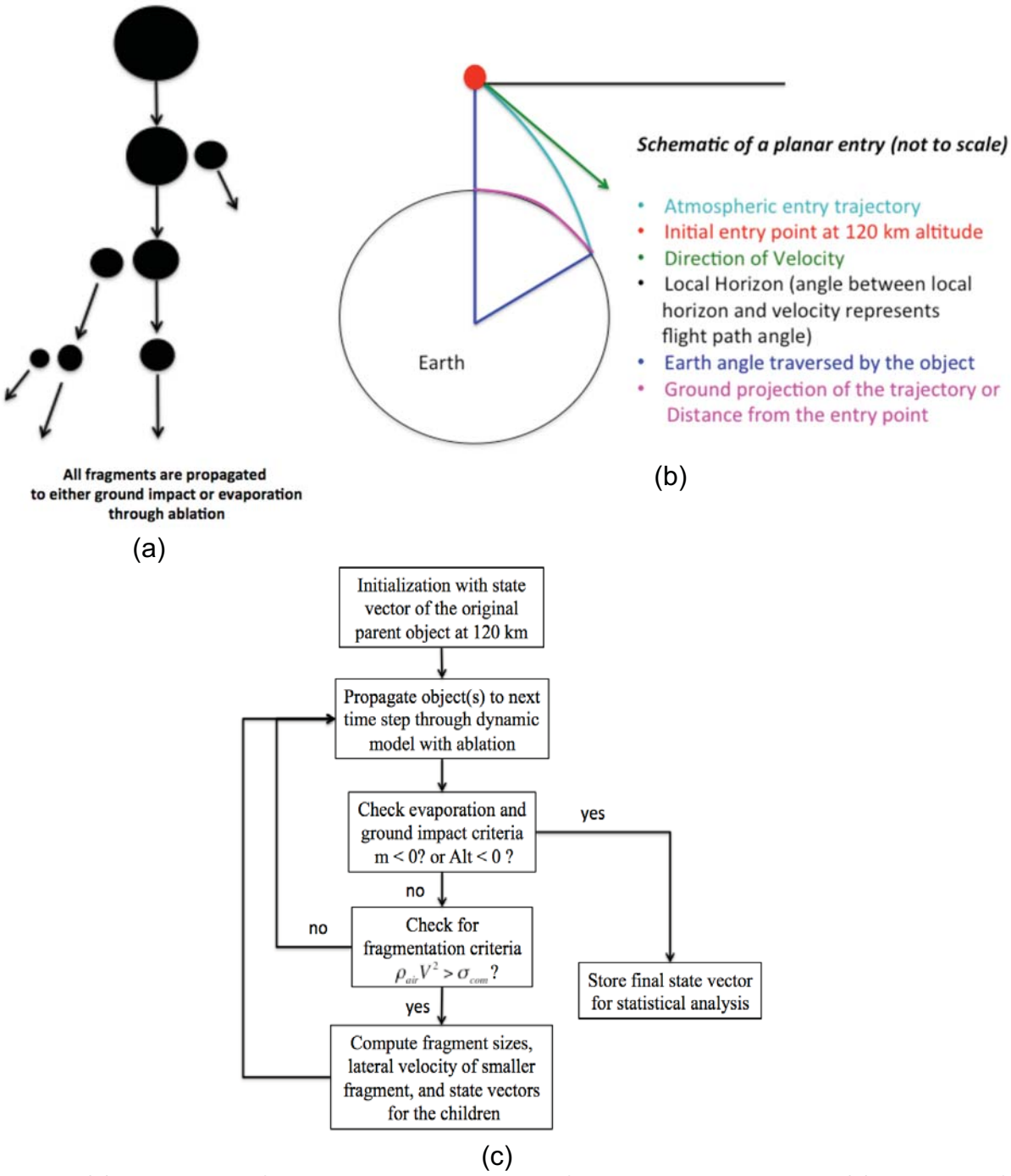

Figure 1: (a) A schematic of the trajectory simulation with fragmentation and ablation, (b) schematic of a planar entry, and (c) developed algorithm for the simulation.

Trajectory Dynamics Model

The object entering the Earth's atmosphere is modeled as a point mass whose dynamics is governed by the following system of differential equations:

$$\dot{h} = V\sin\gamma \tag{1}$$

$$\dot{V} = -\frac{D}{m} - g\sin\gamma + \omega_E^2(R_E + h)\cos\phi(\sin\gamma\cos\phi - \cos\gamma\cos\chi\sin\phi) \tag{2}$$

$$\dot{\gamma} = \left(\frac{V}{R_E + h} - \frac{g}{V}\right)\cos\gamma + 2\omega_E \sin\chi\cos\phi + \omega_E^2\left(\frac{R_E + h}{V}\right)\cos\phi(\cos\chi\sin\gamma\sin\phi + \cos\gamma\cos\phi) \tag{3}$$

$$\dot{\chi} = -\left(\frac{V}{R_E + h}\right)\cos\phi\sin\chi\tan\phi + 2\omega_E(\sin\phi - \cos\chi\cos\phi\tan\gamma) - \omega_E^2\left(\frac{R_E + h}{v\cos\gamma}\right)\cos\phi\sin\gamma\sin\chi \tag{4}$$

$$\dot{\phi} = \left(\frac{V}{R_E + h}\right)\cos\gamma\cos\chi \tag{5}$$

$$\dot{\lambda} = \left(\frac{V}{R_E + h}\right)\frac{\cos\gamma\sin\chi}{\cos\phi} \tag{6}$$

where h is the altitude, V is the speed of the object, γ is the flight path angle, D is the drag force, g is the gravitational acceleration, ω_E is the Earth's rotational speed, R_E is the radius of the Earth, χ is path direction angle, and ϕ and λ are latitude and longitude respectively. The gravitation acceleration is modeled as a function of the altitude given as:

$$g(h) = g_0\left(\frac{h}{R_E + h}\right)^2 \tag{7}$$

where the g_0 is 9.81 m/s^2.

Hypersonic Aerodynamics

A simple sphere model is used for the object geometry. Since most of the atmospheric entry occurs at the high hypersonic regime where the drag coefficient is independent of the value of the Mach number, we assume a value of 0.92 for the drag coefficient given by Modified Newtonian Theory [13]. To account for uncertainty, we model the drag coefficient as a random variable with uniform distribution centered on 0.92. Acceleration due to drag acting on the object used in Eq. (2) is calculated using the standard theoretical drag model given as:

$$a_{drag} = \frac{D}{m} = -\frac{1}{2}\rho_{air}\frac{C_D A}{m}V^2\frac{V}{|V|} \tag{8}$$

where ρ_{air} is the atmospheric density, C_D is the drag coefficient, A is the cross sectional area, and m is the mass of the object. Since the entering object is modeled as a sphere, we assume the nature of the motion to be planar (lift and side forces are neglected). It should be noted however, that the developed framework allows for addition of lift and side forces by implementing small changes in the dynamics model.

Atmospheric Density

The atmospheric density, ρ_{air}, is computed using an interpolation routine that is developed using data from the US standard atmosphere. Values (mean and standard deviation) at a series of altitudes are obtained from the US standard atmosphere. We assign Gaussian distributions to the data at these altitudes, which allow draws from the distributions for every Monte Carlo sample. Densities at altitudes other than those with data points are computed using piece-wise linear interpolation in the logarithmic scale. The values in the US standard atmosphere are provided to an altitude of about 90 km. The mean value at 120 km was read of the US standard atmosphere table and the standard deviation was assumed to be the same as at 90 km. Figure 2 shows 1000 samples drawn from the density interpolation routines, constrained to the data points. Every run of the Monte Carlo sample uses one of the data lines shown in Figure 2 for propagation of trajectory from entry to ground.

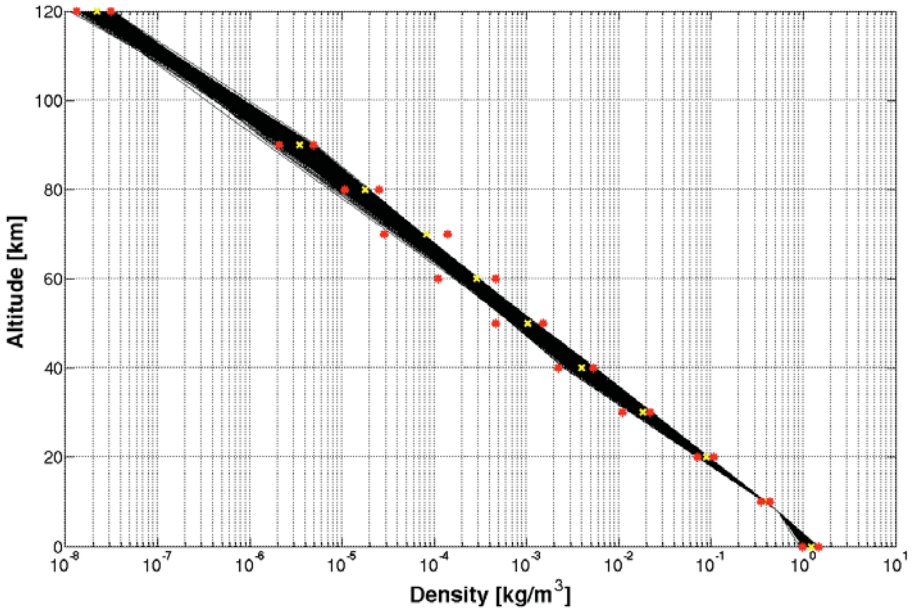

Figure 2: 1000 samples from the density interpolation routine. The yellow and red data points represent the mean and standard deviation, respectively.

Ablation Model

The rate at which the object material mass is ablated is calculated using the following relationship:

$$\dot{m} = -\frac{(Q_R + Q_C)}{Q_{ab}} \tag{9}$$

where Q_{ab} is the effective heat of ablation, and Q_R and Q_C are effective radiative and convective heat transfer values, respectively.

Brandis et al., [9] give the correlations for the stagnation point convective and radiative heat flux for objects with finite radius of curvature as a function of ρ_{air} and v. Convective heat flux correlations are given for a speed range of 3 to 17 km/s, whereas radiative heat flux correlation is only available for a speed range of 9.5 to 17 km/s. The correlations are only valid for densities between 1e-5 and 5e-3 kg/m^3 and radius of curvature between 0.2 and 10 m. Radiative heat transfer is assumed to be

zero at speeds between 3 and 9.5 km/s and no heat transfer is included under speeds of 1.5 km/s.
At entry conditions other than the ones described above, we use the analytical and theoretical models for stagnation point convective and radiative heat flux. The convective heat flux is computed using the Fay-Riddell relation given as [14]:

$$\dot{Q}_C = 0.94(\rho_w \mu_w)^{0.1}(\rho_s \mu_s)^{0.4}(h_s - h_w)\sqrt{\left(\frac{du_e}{dx}\right)_s} \tag{10}$$

where [ρ_w, ρ_s], [μ_w, μ_s], and [h_w, h_s] are density, viscosity, and enthalpy at the wall and stagnation point, respectively, and the last term is the velocity gradient at the stagnation point computed as:

$$\sqrt{\left(\frac{du_e}{dx}\right)_s} = \frac{1}{r_N}\sqrt{\frac{2(p_s - p_\infty)}{\rho_s}} \tag{11}$$

where (du_e/dx) is the velocity gradient, and p_s and p_∞ are stagnation point and free stream pressure, respectively.
The radiative heat flux is computed using the theoretical model given as:

$$\dot{Q}_R = \sigma k T_{shock}^4 \tag{12}$$

where σ is the emissivity, k is the Boltzmann constant, T_{shock} is the gas temperature just downstream of the shock. The temperature just downstream of the shock or the shock layer temperature for radiative heat flux is computed by extrapolating the relation of Anderson [15] for chemically reacting gas in equilibrium to NEO re-entry velocities and assuming radiative equilibrium at ~25K Kelvin. Anderson's relation and the model used in the module are shown in Figure 3.

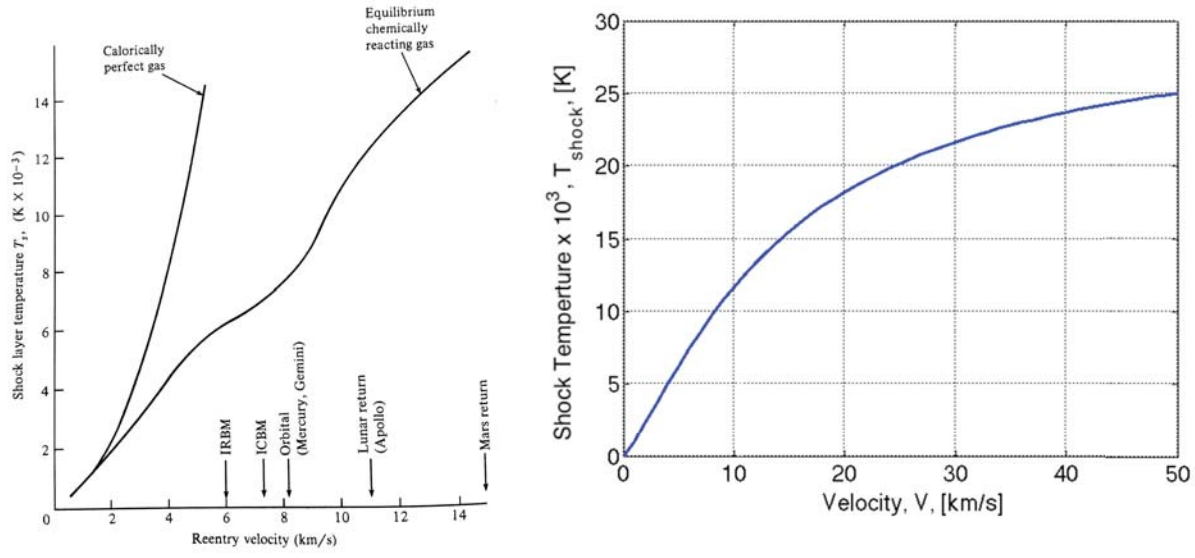

(a) (b)

Figure 3: a) Shock layer temperature a chemically reacting gas in equilibrium as a function of velocity as given by Anderson [15], and (b) Anderson's shock layer temperature extended to possible NEO re-entry velocities.

Based on several high fidelity simulations with the Direct Simulation Monte Carlo (DSMC) and Computational Fluid Dynamics (CFD), the total effective heat transfer to

a spherical object is taken to be approximately about 5% of the stagnation point heat flux. Therefore, rate of ablation becomes:

$$\dot{m} = -\frac{0.05 \cdot \left(\dot{Q}_R + \dot{Q}_C\right)}{Q_{ab}} \tag{13}$$

Successive Fragmentation Model

A fragmentation event is modeled as a function of the stagnation pressure of the airflow free stream and the compressible strength of the asteroid material. A fragmentation occurs is the dynamic pressure exceeds the compressive strength of the material [11]:

$$\rho_{air} V^2 > \sigma_{com} \tag{14}$$

where σ_{com} is the compressive strength of the parent object. The compressive strength of the original parent object and the relative size of the fragmented pieces after each event are treated as uncertain parameters.

Each fragmentation event is assumed to result into only two children, which allows significant simplification of the problem. The size of the smaller fragment after each fragmentation event is modeled with a uniform distribution in the size range of 5 – 45% of the parent. This particular range is considered in order to cover the entire spectrum where the lateral velocity models are applicable while avoiding extreme points. These models are discussed in detail in the next section. The number of successive fragmentation events are not limited but are based solely on the condition in Eq. (14) and the post-fragmentation structural strength of the pieces calculated using the model of Weibull [16] as follows:

$$\sigma_c = \sigma_p \left(\frac{m_p}{m_c}\right)^{\alpha} \tag{15}$$

where $[\sigma_c, \sigma_p]$ and $[m_c, m_p]$ are compressive strength and mass of the child and parent, respectively, and α is a scale factor. The scale factor, α, is another parameter considered uncertain.

Fragment Interaction and Lateral Velocity Model

Each progressive fragmentation event is assumed to result in only 2 children, one that continues along the trajectory of the parent and the second that is given a small lateral velocity relative to the parent. The second child element is assumed to always be smaller than the parent after fragmentation. The lateral velocity of separation of the child in calculated based on the following relation of Passey and Melosh [17]:

$$V_T = \sqrt{C \frac{r_1}{r_2} \frac{\rho_{air}}{\rho_m}} V \tag{16}$$

where V_T is the final lateral velocity, C is a constant that Passey and Melosh [17] determined through examination of various terrestrial crater fields to lie between 0.03 and 2.5, r_1 is the size of the larger fragment, r_2 is the size of the smaller fragment, and ρ_m is the object material density.

Laurence et al., [12] performed an experimental and computational investigation into the unsteady separation behavior of two spherical objects under aerodynamics. Using experimental and computational analysis they derived the normalized separation velocity as a function of the ratio of the size of the fragments. Figure 4 shows the normalized separation velocity as a function of the fragment size ratio and Mach number.
The data of Laurence et al., [12] is extrapolated to Mach Numbers typical of asteroids. We assume an asymptotic convergence to the solution for higher Mach (velocities) to Mach 25 values. The normalized separation velocity is used to compute the constant *C* using the following relationship:

$$C = V_T'^2 \frac{r_2}{r_1} \tag{17}$$

which is then used to compute the Lateral velocity as per the model of Passey and Melosh [17].

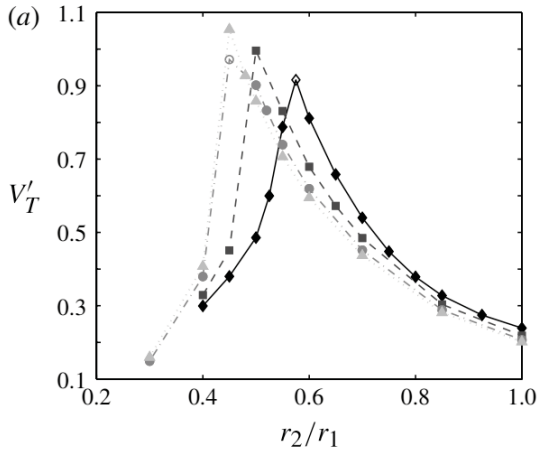

Figure 4: Normalized separation velocity as a function of fragment size ratio. diamond, M = 4; square, M = 6; circle, M = 10; triangle, M = 25 [17].

RESULTS AND DISCUSSION

The break-up and ablation modeling and trajectory simulation is performed under atmospheric and object property uncertainties. Since a large number of the parameters that have an influence on the atmospheric entry of NEO's are uncertain, we perform a Monte Carlo analysis to get the probabilistic distributions for the parameters of interest. The primary focus of such an analysis is to get a probabilistic representation of the ground impact location towards the decision-making process for casualty avoidance.

We run a Monte Carlo with 10,000 samplings to get accurate representative distributions of a simulated asteroid atmospheric entry scenario. We use representative object and re-entry parameters of the small celestial body that entered the Earth's atmosphere over the Chelyabinsk region of Russia back in February 2013. We assume an object initial diameter size of 20-meter. Table 1 gives the list of considered uncertain parameters and the associated distribution type with

mean and limiting values. Each of the uncertain parameters has been discussed in detail in their respective previous sections.

Table 1: Uncertain Simulation Parameters

Parameter	Distribution	Deterministic/ Nominal Value	Min Value	Max Value
Entry Velocity (km/s)	Uniform	20	15	25
Flight Path Angle, deg	Uniform	-15	-10	-20
Direction Angle, deg	Uniform	90 (due east)	89	91
Initial Mass (kTon)	Uniform	10	9	11
Drag coefficient, C_D	Uniform	0.92	0.5	1.34
Object strength, σ_{com} (MN/m^2)	Uniform	20	10	30
Object density, (kg/m^3)	Uniform	3500	3000	4000
Strength Scale factor, α	Uniform	0.3	0.1	0.5
Heat of ablation, (MJ/kg)	Uniform	9	8	10
Hot gas emissivity	Uniform	0.05	0.01	0.09

Results of two sensitivity studies are presented, one for the effect of the value of *C* in Eq. (16) and the other for the effect of the flight path angle. Sensitivity studies to other parameters can be easily performed as desired. Figure 5 and 6 show the results for the case of using the model of Laurence et al., (2012) in the computation of lateral velocities and the uncertain parameters and distributions listed in Table 1. Figure 5(a) shows the distribution of the mass of the impacting fragments. The largest fragment with a possibility of reaching the ground is close to about 20% of the initial object at 2x10^6 kg. Figure 5(b) shows the average impact mass per unit area of the impacting fragments in ~80km^2 (~40 km longitudinal x ~2 km lateral bins) of area. The highest mass density is around the nominal solution at about 400 km downstream of the entry point. The nominal solution is where the object is expected to impact in the absence of any uncertainty. The mass density decreases both longitudinally and laterally away from the nominal zone with densities spanning 6 orders of magnitude across the distribution. This distribution can be used in making evacuation decisions. This distribution can also be used in combination with the population density to derive the extremity of the possible casualties. The average total mass reaching the ground in this case is about 5.98x10^6 kg (which is 60% of the average initial mass).

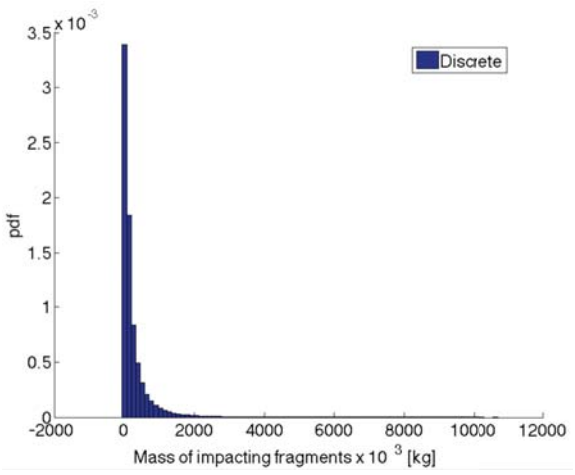

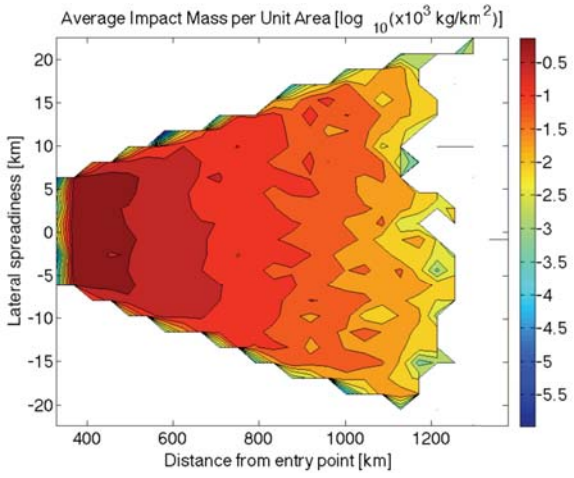

(a) (b)

Figure 5: **(a)** Probabilistic distribution of the mass of impacting fragments. (d) Distribution map of the impact mass per unit area.

Figure 6(a) shows the probabilistic distribution for the longitudinal impact distance from the point of entry. The nominal solution seems to lie at about 400 km with possible fragment impacts between about 350 and 1200 km. The steep drop towards the tail (from ~500 to ~1000 km) can be characterized by the second order effect of velocity on drag as given in Eq. (8). The figure also shows an equivalent Gaussian distribution derived from the properties (mean and standard deviation) of the actual probability function. Comparing the two shows that the actual distribution is quiet far from a Gaussian that is typically assumed. Figure 6(b) shows the probabilistic distribution for the lateral impact distance. Results show that the nominal/deterministic solution lies along the center of the direction angle distribution. Comparing the distribution with the equivalent Gaussian shows that a Gaussian can provide a decent estimate of the lateral spread, however it cannot take into account the plateau feature towards the peak. Understanding the cause of such a feature is beyond the scope of this work, however, it will be a subject of future work. Figures 6(c) and 6(d) show the 2D representation of the lateral and longitudinal distribution of the total number of impacts over the complete Monte Carlo sample. The 2D representation shows that the lateral and longitudinal distributions are tied together and cannot independently represent the impact footprint. Results show that the lateral distribution starts close to about 10 km at the nominal longitudinal solution diverging to about 25 km close to the longitudinal tail. It should be noted that the distributions have not reached a steady state or convergence even with 10000 runs as the fragmentation events add a high level of complexity to the problem; however, for the purposes of decision-making, it provides sufficient knowledge.

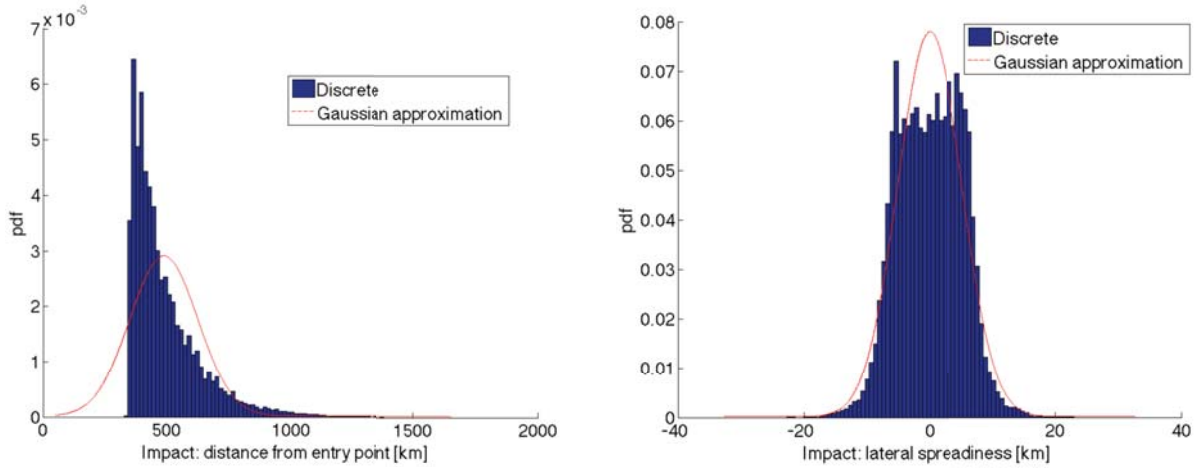

(a) (b)

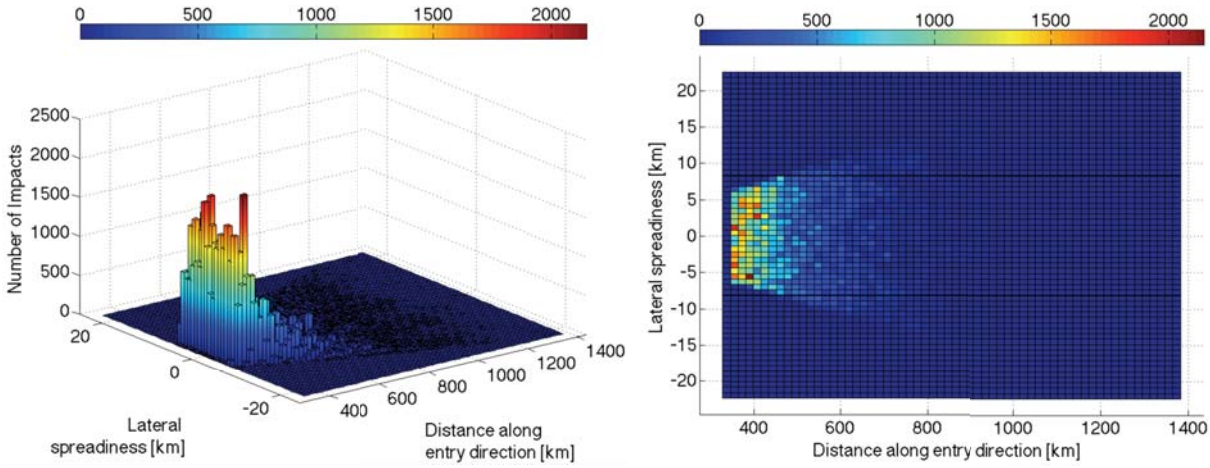

(c) (d)

Figure 6: (a) Probabilistic distribution of the impact distance from the point of entry, (b) Probabilistic distribution of the lateral spread distance, (c) a 2D histogram of the longitudinal and lateral distribution, and (d) top view of the 2D histogram.

Effect of the parameter *C*

Figures 6 and 7 show the results for the effect of the parameter *C* in Eq. (16) on the ground impact distribution. Comparing the distributions in Figure 6(d) (Laurence et al., for value of *C*) with those in Figure 7(b) (*C* = 0.1) and Figure 7(d) (*C* = 2.5) shows that the values of C has a negligible effect on the ground impact distribution. This is because the uncertainty/variation in the direction angle dominates the lateral distribution. This dominating effect can be deduced from the 2D distribution in Figure 8 where a constant value of the direction angle (90 deg) is used in place of a uniform distribution accounting for uncertainty. It should be noted that the distributions in Figures 8(a) and (b) are identical with same scale in the longitudinal direction, however, the lateral distribution in Figure 8(b) is about 4 times wider than in 8(a). Comparing figures 7(a) and 7(b) shows that the difference in limits of the lateral distribution can vary by an order of magnitude depending on the value of *C*. Comparing figures 7(b) with 8(a) and figure 7(d) with 8(b) also shows that the direction angle uncertainty can dominate the lateral distribution limits by up to 2 orders of magnitude.

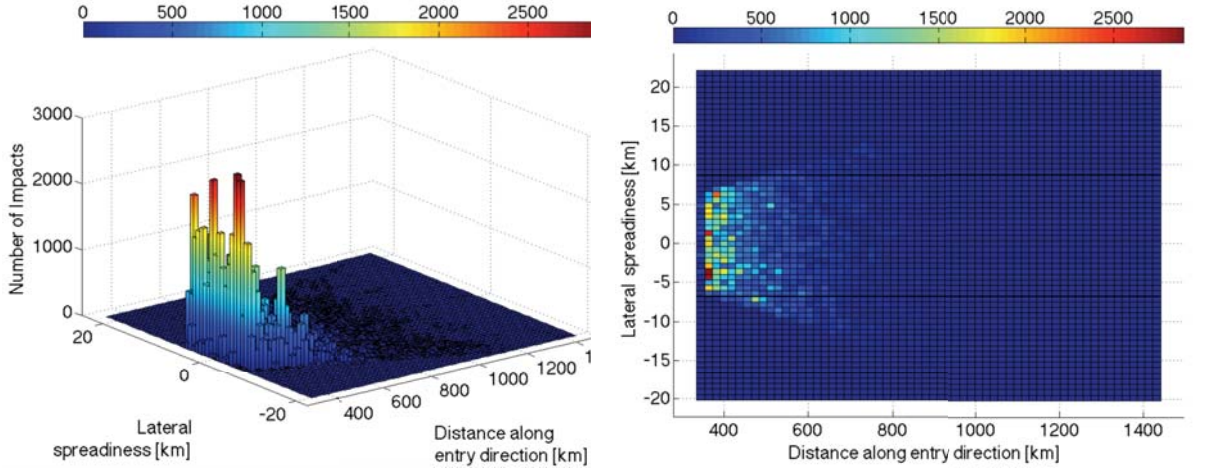

(a) (b)

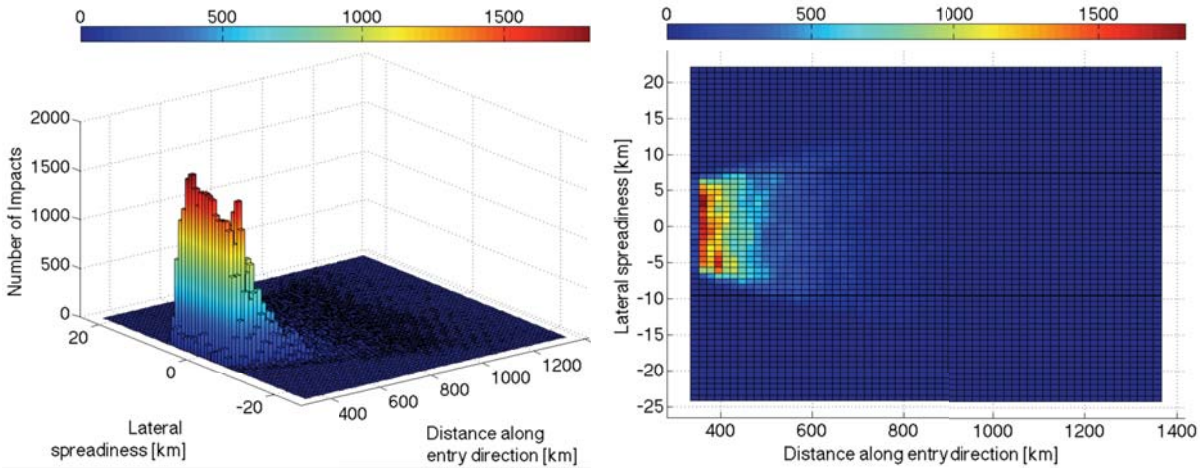

(c) (d)

Figure 7: (a) a 2D histogram of the longitudinal and lateral distribution for *C* = 0.1, (b) top view of the 2D histogram for *C* = 0.1, (c) a 2D histogram of the longitudinal and lateral distribution for *C* = 2.5, and (d) top view of the 2D histogram for *C* = 2.5.

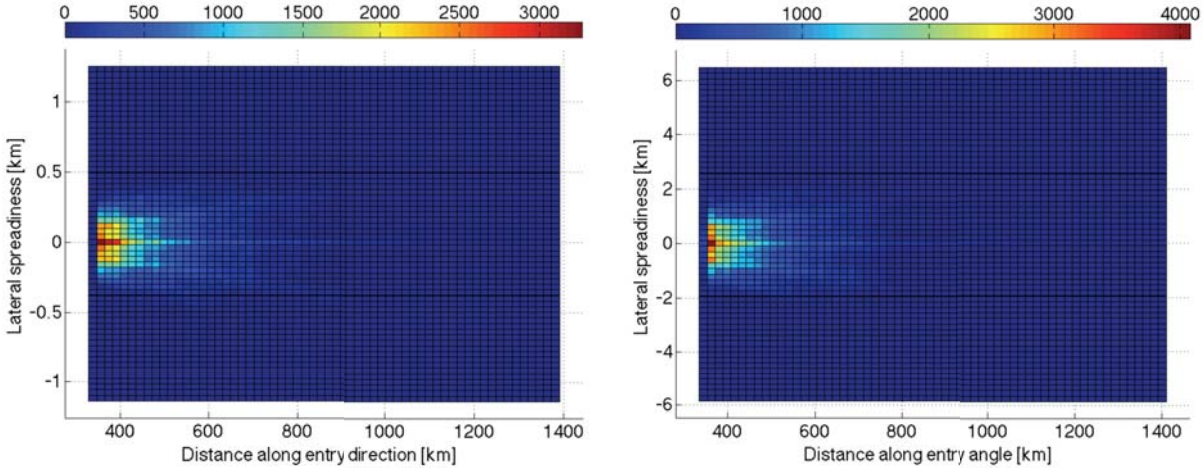

(a) (b)

Figure 8: (a) top view of the 2D histogram for *C* = 0.1 neglecting uncertainty in the direction angle, and (b) top view of the 2D histogram for *C* = 2.5 neglecting uncertainty in the direction angle.

Effect of the Flight Path Angle

Figures 9 and 10 show the results for the case of using the model of Laurence et al., (2012) in the computation of lateral velocities and the uncertain parameters and distributions listed in Table 1 but for a flight path angle of -45 deg. Figure 9(a) shows the distribution of the mass of the impacting fragments. The largest fragment with a possible impact is only about 5% of the initial starting mass as opposed to 20% for the shallower case with the mean value of less than 0.05×10^6 kg (less than 0.5% of the initial mass). Figure 9(b) shows the average impact mass per unit area of the impacting fragments in ~0.4km^2 (~2 km longitudinal x ~0.2 km lateral bins) of area. The distribution is much more uniform compared to the shallower case. The average total mass reaching the ground in this case is about 4.50×10^6 kg, approximately 10 – 15% smaller than the shallower case.

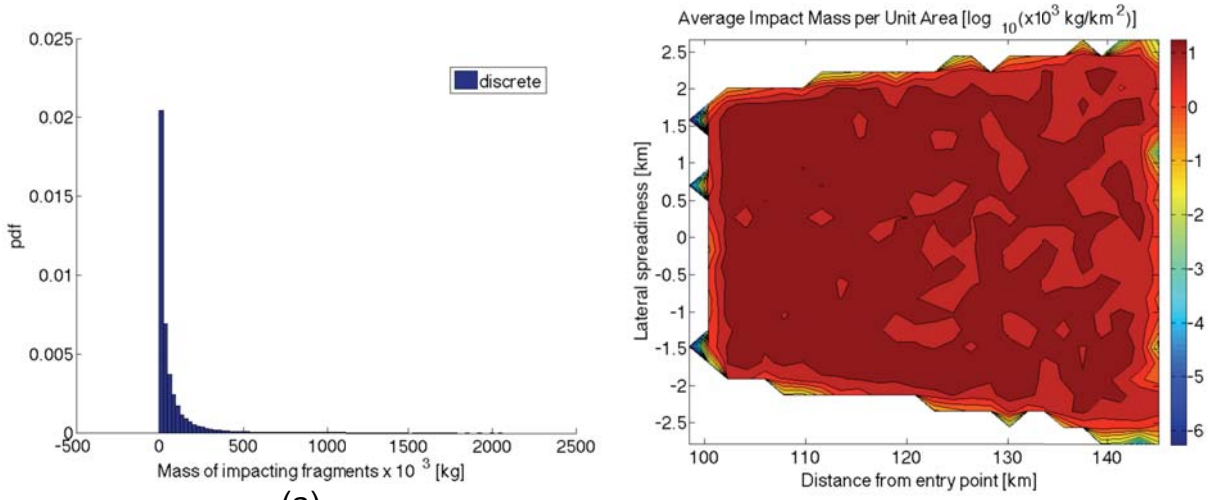

(a) (b)

Figure 9: **(a)** Probabilistic distribution of the mass of impacting fragments. (d) Distribution map of the impact mass per unit area.

Figure 10(a) shows the probabilistic distribution for the longitudinal impact distance from the point of entry. The nominal/deterministic solution seems to lie at about 105 km as compared to about 400 km for the shallower case. The spread is also reduced to about 40 km down from about 850 km for the shallower case. The drop towards the tail is also not as steep as the shallower case because the object spends a much smaller time encountering aerodynamic forces that causes the second order effect due to velocity. Figure 10(b) shows the probabilistic distribution for the lateral impact distance. Results show that the nominal/deterministic solution lies along the center of the direction angle distribution. Once again, the actual distributions are far from a Gaussian that is typically assumed. Figures 10(c) and 10(d) show the 2D representation of the lateral and longitudinal distribution of the total number of impacts over the complete Monte Carlo sample. The lateral spread is reduced by up to an order of magnitude compared to the shallower case. It should also be noted that due to the steep entry angle, each Monte Carlo run produces, on average, fragments that are an order of magnitude more than the shallower case.

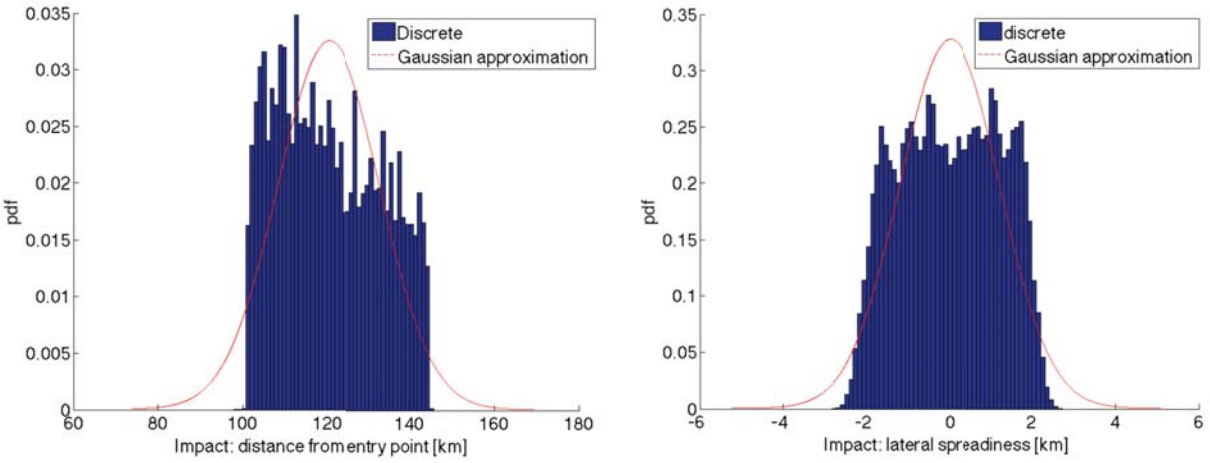

(a) (b)

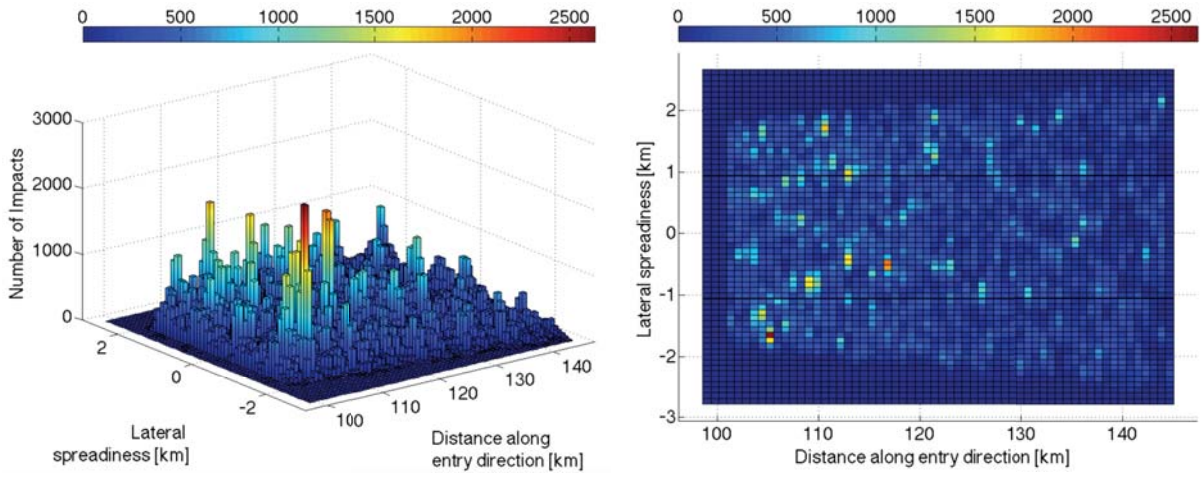

(c) (d)

Figure 10: (a) Probabilistic distribution of the impact distance from the point of entry, (b) Probabilistic distribution of the lateral spread distance, (c) a 2D histogram of the longitudinal and lateral distribution, and (d) top view of the 2D histogram.

Computational Requirements

The framework is developed for use with Matlab®. For all the different cases presented here the average computational time for each sampling is around 50/60 seconds. Some runs for the case of flight path angle of -45 deg takes just 3/4 of a second whereas other runs can take close to 600 seconds. For running a sample of 10,000 members in series, the sampling would require nearly 150 hours on "Dual Intel Xeon X5650 2.66 GHz CPU's". The cases for this work were run in parallel and completed in just under 3 hours. The computational time is related to the ODE step-size and method. The method used in this work is an Adams 4^{th} order predictor-corrector and the step-size is 1e-2 seconds. Future work will include implementation of a High Dimensional Model Representation (HDMR) based approach to reduce the computational time by a factor up to 2 orders of magnitude (expected based on other applications) [18].

CONCLUSIONS

We have presented results from a tool that is developed for the primary goal of decision making towards casualty avoidance during an asteroid or meteorite entry event. The tool can model and simulate ablation, burn-up/evaporation, fragmentation, pre- and post- fragmentation event trajectories and ground impact footprint for asteroids as a result of the associated uncertainties. We have developed a framework, which implements state-of-the-art models available today that can be updated as desired. Studies are performed to characterize the sensitivity of the distribution of the parameters of interest to two uncertain parameters, the coefficient C in the fragment interaction and lateral velocity model and the flight path angle, γ. The value of C is has been deduced by pervious studies to fall in the range of 0.1 to 2.5. Laurence et al., (2014) recently also developed a model to compute the value of 'C' based on experimental and computational simulations. Results indicate that the uncertainty in the direction angle, χ, masks the effect of C and the value of C becomes irrelevant for the application of ground impact distribution. However, in the

event of very low uncertainty in the direction angle, χ, which could be the case closer to actual impact time, the limits on the value of C (0.1 and 2.5) can produce lateral distributions that can differ by up to an order of magnitude.

The effect of the flight path angle, γ, was studies with simulations performed at mean values of -15 and -45 degrees. Results show that a steeper entry angle of -45 deg reduces the longitudinal spread of the distribution down to about 40 km from about 850 km for the shallower angle. The longitudinal distributions also show that for the steeper case, the steep decline in the distribution away from the nominal solution and towards the tail is reduced because of the smaller time spent in the aerodynamics regime that causes a second order effect due to velocity. The lateral distribution is also reduced in the case of a steeper entry angle by up to an order of magnitude.

The developed framework and tool can be used by decision-makers for decisions concerning mitigation and evacuations for casualty avoidance in the case of a near Earth object being unobservable until too late or if it manages to survive the deflection attempts. Future work will include the use of the tool in characterizing the properties of object and its orbit based on observed ground impact distribution. The tool is also available freely to anyone who wishes to use it. Interested users are encouraged to contact the primary author for access to the tool.

ACKNOWLEDGEMENT

Funding for Piyush Mehta is provided by the European Commission through the Marie Curie Initial Training Network (ITN) STARDUST under grant number 317185. The authors would like to acknowledge the use of the High Performance Computing Resources 'ARCHIE' at the University of Strathclyde.

REFERENCES

1. Popova, Olga P.; Jenniskens, Peter; Emel'yanenko, Vacheslav; et al. (2013). "Chelyabinsk Airburst, Damage Assessment, Meteorite Recovery, and Characterization". *Science* 342 (6162): 1069–1073. doi:10.1126/science.1242642.
2. Schiermeier, Quirin, Risk of massive asteroid strike underestimated, *Nature News*, Nature Publishing Group, Nov 2013.
3. Cooke, William, Orbit of the Russian Meteor, *NASA blogs*, Feb 2013.
4. Malik, Tariq, Russian Meteor Blast Bigger Than Thought, NASA says, *Huffington Post*, Feb 2013.
5. Baldwin B, Sheaffer Y, Ablation and breakup of large meteoroids during atmospheric entry. JGR, Vol. 76, No. 19, 1971, pp. 4653-4668.
6. Stulov VP, Analytical model of consecutive breakup and ablation of a meteor body in the atmosphere, Astron Bull, Vol. 32, No. 5, 1998, pp. 455-458.
7. Artemieva NA, Shuvalov VV, Fragmented meteoroid movement through the planetary atmosphere, JGR, Vol. 106, 2001, pp. 3297-3310.
8. Zhdan IA, Stulov VP, Stulov PV, Aerodynamic interaction of two bodies in a supersonic flow, Dokl Phys, Vol. 49, No. 5, 2004, pp. 315-317.
9. Brandis, A. M., and Johnston, C. O., Characterization of Stagnation-Point Heat Flux for Earth Entry, 45th AIAA Plasmadynamics and Lasers Conference, AIAA Aviation, Atlanta, 16-20 June 2014.
10. Bronshten, V. A., Physics of Meteoric Phenomena, Nauka, Moscow, 1981.

11. Tsvetkov V. I., and Skripnik, A. Y., Atmospheric fragmentation of meteorites according to the strength theory, Sol. Syst. Res., 25, 1991, pp. 273-279.
12. Laurence, S. J., Parziale, N. J., and Deiterding, R., Dynamical separation of spherical bodies in supersonic flow, J. Fluid Mech., Vol. 713, 2012, pp. 159-182.
13. Newton, I., Principia – Mote's Translation Revised, University of California Press, 1946.
14. Fay, J. A., and Riddell, F. R., "Theory of Stagnation Point Heat Transfer in Dissociated Air," *Journal of the Aeronautical Sciences*, Vol. 25, No. 2, 1958, pp. 73–85.
15. Anderson, J.D., Hypersonic and High Temperature Gas Dynamics, AIAA, 1989.
16. Weibull W., A statistical distribution function of wide applicability, J. Appl. Mech., 10, 1951, pp. 140-147.
17. Passey, Q. R., and Melosh, H. J., Effects of atmospheric breakup on crater field formation, Icarus, 42(2), 1980, pp. 211-233.
18. Kubicek, M., Minisci, E., Cisternino, M., High dimensional sensitivity analysis using surrogate modeling and High Dimensional Model Representation, International Journal for Uncertainty Quantification, accepted, April 2015.